ChemComm

ROYAL SOCIETY OF CHEMISTRY

COMMUNICATION

View Article Online
View Journal | View Issue

Cite this: *Chem. Commun.*, 2023, 59, 5753

Received 6th March 2023,
Accepted 13th April 2023

DOI: 10.1039/d3cc01110k

rsc.li/chemcomm

Nitroreductase-sensitive fluorescent covalent organic framework for tumor hypoxia imaging in cells†

Tina Skorjanc, *[a] Dinesh Shetty, *[bc] Sushil Kumar, [b] Damjan Makuc, [d] Gregor Mali, [d] Janez Volavšek, [d] Martina Bergant Marušič [e] and Matjaz Valant [a]

Covalent organic frameworks (COFs) have been used in cell imaging, but very rarely for imaging specific cell conditions. Herein, a β-ketoenamine-based fluorescent COF was post-synthetically modified to incorporate a hypoxia-targeting molecule. Fluorescence microscopy imaging shows that the material discriminates between HeLa cells grown under hypoxia and those cultured under normoxia.

Hypoxia is a physiological condition characterized by low pO_2 that results from an inadequate supply of oxygen to cells and/or tissues. It is commonly encountered in solid tumors and in diseases such as ischemia and atherosclerosis.[1] Solid tumors have a median O_2 level of 4%, yet locally this number can drop to nearly 0%.[2] Monitoring the condition of hypoxia is important as it, for instance, allows for early-stage cancer diagnostics while other medical imaging tools require comparably larger sizes of tumors for diagnostics.[3] Furthermore, detecting hypoxia is also relevant in the pathogenesis of chronic renal disease, progression of rheumatoid arthritis, and blood vessel plaque vulnerability.[4]

Various methods of both invasive and noninvasive hypoxia imaging have been developed.[5] The much preferred non-invasive hypoxia imaging traditionally relies on magnetic resonance imaging (MRI), electron paramagnetic resonance (EPR), or positron emission tomography (PET). More recently, fluorescence imaging has likewise received significant attention in the realm of cancer imaging on account of its high sensitivity, low toxicity, good spatial and temporal resolution, emission tunability, simple operation, and non-invasive nature.[6] Fluorescent probes for hypoxia imaging often target cancer markers, in particular hypoxia-related reductase enzymes. In the hypoxic tumor microenvironment, reductases, such as azo reductase and nitro reductase, are overexpressed. While the azo group is an azo-reductase-sensitive moiety, nitro-imidazole is a nitro-reductase-sensitive moiety.

Various small-molecule fluorophores have been developed for imaging hypoxic conditions[7] yet it is the nanomaterials that enable passive tumor accumulation and retention due to the enhanced permeability and retention (EPR) effect.[8] This prompted the investigation of various nanomaterials for hypoxia imaging,[9] but the ideally suited covalent organic frameworks (COFs) have been overlooked. Due to their purely organic nature, structural and functional tunability, and porosity, which could also be exploited for drug delivery, COFs are strong candidates for the imaging of cellular conditions.

Only a few examples of COFs have been studied for bioimaging where cell imaging is primarily achieved using the inherent fluorescence of the materials,[10,11] or relying on the fluorescence of a conjugated moiety, such as dye-labeled nucleic acids[12,13] and fluorescent probes.[14] Reports of COFs for imaging any kind of specific cellular conditions are even scarcer.[15] Herein, we design and characterize a COF with a nitroreductase-sensitive moiety for fluorescence imaging of hypoxia. We synthesize a fluorescent COF with the aid of β-ketoenamine chemistry,[16] and post-synthetically modify it to conjugate a nitroimidazole for targeting nitroreductases in tumor hypoxia condition. 2-Nitroimidazole derivatives are electron-deficient compounds known to act as exogenous hypoxia markers that undergo bioreductive activation followed by selective entrapment in hypoxic cells (Fig. S1, ESI†).[17] Thus-obtained nitroimidazole COF (**NI-COF**) is stable in physiological conditions and exhibits useful fluorescence properties with an emission peak at 480 nm (λ_{ex} = 420 nm) at both neutral pH and in acidic pH levels characteristic of tumor tissues. Taking advantage of its low cytotoxicity, we implemented **NI-COF** as a fluorescence imaging

[a] *The Materials Research Laboratory, University of Nova Gorica, Vipavska 11c, Ajdovscina 5270, Slovenia. E-mail: tina.skorjanc@ung.si*
[b] *Department of Chemistry, Khalifa University, P.O. Box 127788, Abu Dhabi, United Arab Emirates. E-mail: dinesh.shetty@ku.ac.ae*
[c] *Advanced Materials Chemistry Center (AMCC), Khalifa University, P.O. Box 127788, Abu Dhabi, United Arab Emirates*
[d] *Slovenian NMR Centre, National Institute of Chemistry, Hajdrihova 19, Ljubljana 1000, Slovenia*
[e] *The Laboratory for Environmental and Life Sciences, University of Nova Gorica, Vipavska 13, Nova Gorica 5000, Slovenia*

† Electronic supplementary information (ESI) available. See DOI: https://doi.org/10.1039/d3cc01110k

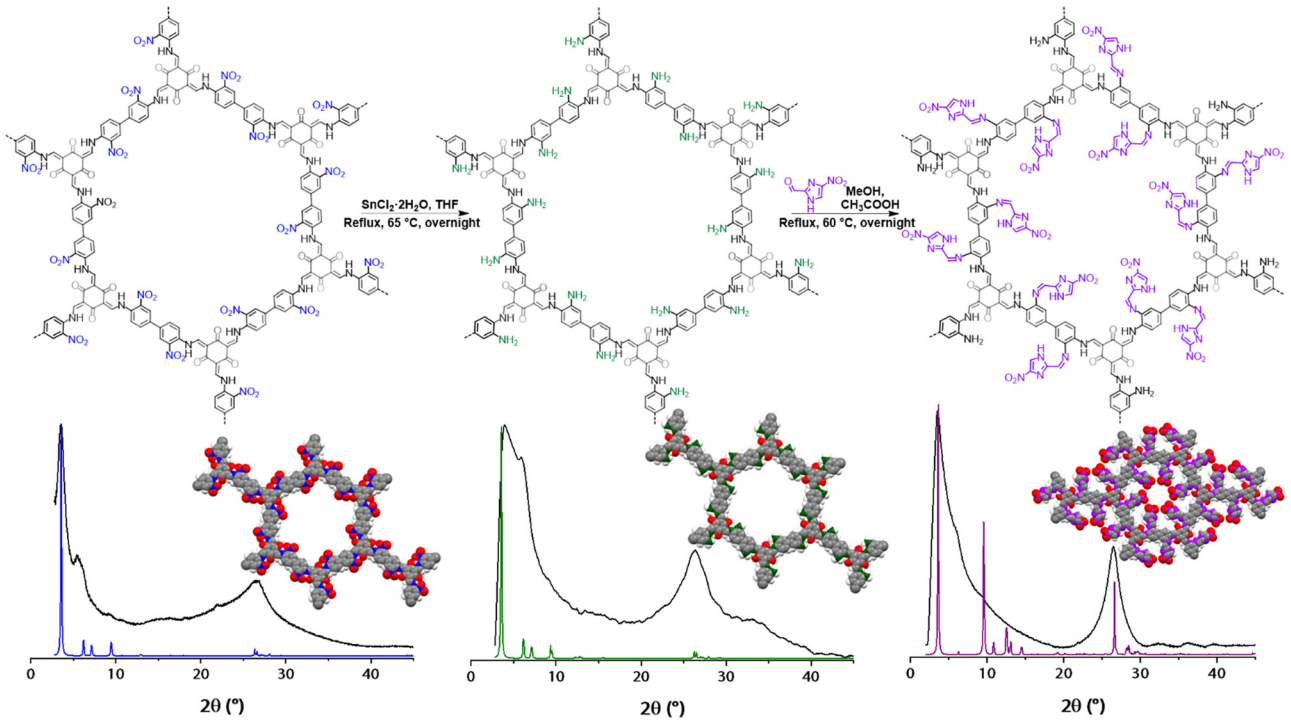

Fig. 1 Synthetic procedure for **NO_2-COF**, **NH_2-COF**, and **NI-COF**, and their corresponding experimental and simulated PXRD patterns.

tool for hypoxia. Our fluorescence microscopy images demonstrate the preferential accumulation of the material in HeLa cells incubated under hypoxic conditions over those incubated under normoxia.

NI-COF was prepared with two post-synthetic modifications of a β-ketoenamine-linked COF prepared from 1,3,5-triformylphloroglucinol (Tp) and 3,3′-dinitrobenzidine (DNB; details in the ESI†). This reaction generated the nitro-functionalized **NO_2-COF** that was subsequently reduced to generate amino-functionalized **NH_2-COF** (Fig. 1; details in the ESI†). In the final step, imine condensation between the amino groups of **NH_2-COF** and the formyl group of 4-nitro-1H-imidazole-2-carbaldehyde (Hyp), a hypoxia targeting molecule, was carried out (Fig. 1, details in the ESI†). All three materials were characterized by standard molecular-level and macroscopic characterization techniques.

Fourier-transform infrared (FT-IR) spectroscopy and solid-state cross-polarization magic-angle spinning (CP-MAS) ^{13}C NMR spectroscopy were used to characterize the materials on the molecular level. In the FT-IR measurements, **NO_2-COF** exhibits three prominent peaks that correspond to N–O stretching at 1514 cm^{-1} and 1338 cm^{-1}, and to NO_2 wagging at 759 cm^{-1} (Fig. 2a). Upon reduction to **NH_2-COF**, these three peaks either disappear entirely or become significantly reduced in intensity. In addition, **NH_2-COF** exhibits a low-intensity peak at 1262 cm^{-1}, which is assigned to the C–N stretching of an aromatic amino group in accordance with the literature.[18,19] Upon conjugating the Hyp molecule to the COF, the FT-IR pattern again changes. The peak at 759 cm^{-1} corresponding to NO_2 wagging re-emerges, and N–O stretching vibrations are visible at 1514 cm^{-1} and 1336 cm^{-1}. A C–N stretching vibration from the Hyp's imidazole is visible at

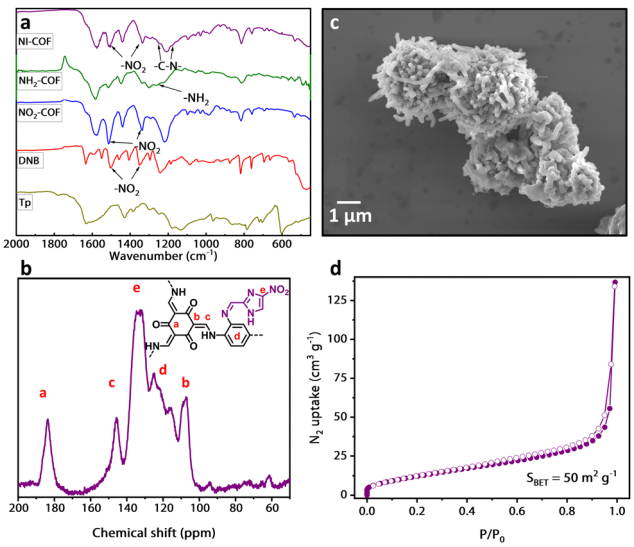

Fig. 2 Characterization of the synthesized materials. (a) FT-IR spectra of the starting materials and **NO_2-COF**, **NH_2-COF**, and **NI-COF**; (b) CP/MAS ^{13}C NMR spectrum of **NI-COF**; (c) SEM image of **NI-COF**, (d) N_2 adsorption isotherm for **NI-COF**.

1247 and at 1150 cm^{-1}.[20] Given the structure of Hyp, these observations strongly suggest successful conjugation of the target molecule to **NH_2-COF**. Solid-state CP-MAS ^{13}C NMR measurements were likewise performed on all COFs to further elucidate their molecular-level structures (Fig. 2b and Fig. S2, ESI†). In **NI-COF**, peaks labelled a, b and c correspond to the carbon atoms adjacent to the keto group (184 ppm), and the two carbon atoms

in the enamine group (145 ppm and 110 ppm), respectively. The broader peaks between 115 ppm and 130 ppm correspond to the aromatic carbon atoms primarily of the linker, while the peak at ~135 ppm is assigned to the $-NO_2$ bound carbon atom of the conjugated targeting molecule.

The structures of all three synthesized COFs were analyzed by powder X-ray diffraction (PXRD), and the resulting PXRD patterns were used to build structural models (Fig. 1 and Fig. S3–S5, ESI†). AA stacking was found to be the preferred conformation in all three COFs. The materials show an intensive reflection at 3.5° that corresponds to the (100) plane. A smaller reflection is observed at 6.0° and assigned to the (110) plane. A broader peak at ~26° is attributed to the (001) plane. These assignments match well with the literature reports.[19] The structure of **NI-COF** was modelled with the eclipsed AA unit cell with the following unit cell dimensions a = 28.0 Å, b = 29.1 Å, and c = 3.37 Å; α = 91.8°, β = 90.4°, and γ = 119.4°. For all three COFs, a Pawley refinement was performed using experimental PXRD pattern. Analysis of results suggests the experimental PXRD pattern is in good agreement with the simulated pattern of eclipsed AA conformation.

Porosity of the synthesized materials was evaluated with N_2 adsorption isotherms at 77 K. All three materials exhibited type I reversible isotherms (Fig. 2d and Fig. S4, ESI†) which attest to the permanent porosity. The Brunauer–Emmett–Teller (BET) surface areas were calculated from the isotherms. In accordance with the literature, the delaminated materials had surface areas of 65, 46 and 50 $m^2\ g^{-1}$ for **NO_2-COF**, **NH_2-COF**, and **NI-COF**, respectively.[16] As has been pointed out in the literature, the keto-enamine based COFs might have lower surface areas than other COFs due to a lower degree of reversibility of this particular chemical reaction.[16] In addition, the incorporation of bulky functional groups into the pores of the materials likewise reduces the surface area. The pore size distributions were calculated using non-local density functional theory (NLDFT). As indicated by the shape of the isotherms, all three materials indeed exhibited microporous nature with the average pore diameter well below 2 nm (Fig. S6, ESI†).

The morphology of the prepared materials was investigated with scanning electron microscopy (SEM) and transmission electron microscopy (TEM). SEM imaging revealed worm-like morphology of the materials that remained largely unchanged upon either of the post-synthetic modifications (Fig. 2c and Fig. S7, ESI†). In the images, these worms aggregate into larger structures, but as discussed below, these can be delaminated into smaller particles. TEM images further confirmed the worm-like morphology at even higher resolution (Fig. S8, ESI†). Thermogravimetric analysis (TGA) was performed on both monomers and on all three COFs to determine their thermal stability (Fig. S9, ESI†). We observe higher thermal stability of the COFs in comparison with individual building blocks up to ~340 °C, an effect that can be attributed to the highly cross-linked nature of the COFs. Furthermore, we notice similar temperature stability in the three COFs, indicating that the post-synthetic modifications performed do not affect the material's thermal stability significantly.

The fluorescence properties of the synthesized materials were studied in aqueous media as all subsequent experiments were performed in biological systems. As described above, each COF was dispersed in water until a stable suspension was obtained and its fluorescence was measured in a 1-cm cuvette. Using the excitation wavelength of 420 nm, emission peaks at around 480 nm were observed in all materials (Fig. S10, ESI†). Tumor tissues commonly experience acidic pH levels, so we also studied the fluorescence properties of **NI-COF** under acidic pH (Fig. S11, ESI†). These measurements confirmed that the fluorescence property is not hampered by mildly acidic (pH = 5) or even highly acidic (pH = 3) environments. Therefore, **NI-COF** is suitable for implementation in hypoxic tumor cell environments that tend to be acidic.

Particle size was studied with dynamic light scattering (DLS) in order to ensure that the particles are sufficiently small for cellular internalization. Delamination was performed with ultrasonic irradiation. This has previously been described as an effective methods for reducing the size of COF particles for biological applications.[10] Such a treatment afforded **NI-COF** particle size to be reduced down to ~165 nm on average (Fig. S12, ESI†). Such particle dimensions are suitable for biological studies, so we proceeded with evaluating the chemical stability of the prepared material in biological media.

Prior to using the material in hypoxia imaging, we tested its stability in phosphate buffered saline (PBS) and in acetate buffer (details in the ESI†). The morphology (Fig. S13, ESI†), chemical composition (Fig. S14, ESI†), and crystallinity (Fig. S15, ESI†) were not affected by these treatments. All these observations considered, we concluded that the material has sufficient chemical and structural stability to be used in biological applications.

A useful imaging agent should exhibit minimal toxicity to cells in order to prevent any effect of the agent on the intracellular processes. To investigate the cytotoxic effects of **NI-COF** and the building blocks from which it was constructed, we resorted to the Presto-Blue™ cell viability assay. **NI-COF** was incubated with HeLa tumor-derived cells at different concentrations up to 300 μg mL^{-1} for 24 hours. Cell viability assay in Fig. S16 (ESI†) shows minimal cytotoxicity of **NI-COF** to HeLa cells as even at a very high concentration of 300 μg mL^{-1} well over 80% of cells remain viable. It should be noted that this exceeds the concentration used for imaging by over seventy-fold. For comparison, the starting materials (DNB and Tp) were also analyzed for cytotoxicity in the same manner (Fig. S16, ESI†), and they similarly exhibited minimal toxicity at low concentrations.

Small particle size, chemical stability in biological media, and very low cytotoxicity of **NI-COF** prompted us to proceed with fluorescence imaging. As detailed in the ESI,† HeLa cells were grown on glass coverslips for 48 hours to ensure that they were well attached. Subsequently the cells were subjected to either normoxic (~20% O_2) or hypoxic environment for four hours. Here, severe hypoxia with O_2 level close to 0% was established. Finally, **NI-COF** was incubated with cells in both types of environments for 60 minutes. After washing with PBS,

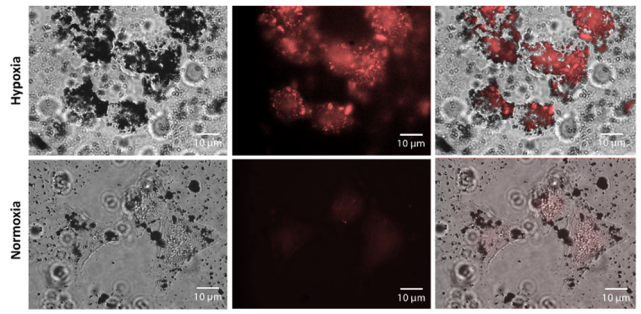

Fig. 3 Fluorescence imaging results for *severe* hypoxia. The top row corresponds to HeLa cells incubated under hypoxia for 4 hours, the bottom row shows HeLa cells incubated under normoxia. [**NI-COF**] = 4 μg mL^{-1}, incubation time 60 minutes. Brightfield, fluorescence and overlay images are displayed.

cells were fixed and imaged. Fig. 3 shows the results obtained for hypoxic and normoxic cells incubated with **NI-COF**, while Fig. S17 (ESI†) shows two additional controls (hypoxic and normoxic cells without **NI-COF** exposure). The controls indicate that the hypoxic treatment itself does not significantly influence cell morphology as in both conditions cells appear healthy and well-formed. While the two controls appear similar to each other, significant differences between **NI-COF**-treated hypoxic and normoxic cells are observed. Cells incubated under normoxic conditions encapsulate only little of **NI-COF**, so they show little-to-no fluorescence signal. In contrast, hypoxic cells show a dramatic uptake of **NI-COF**, resulting in bright fluorescence of the cells.

The same imaging experiment was also conducted in mild hypoxia, where the final O_2 concentration was ~5%. Very similar observations to those described for severe hypoxia can be noted. The controls in hypoxic and normoxic conditions show similar cell morphology and no fluorescence signal (Fig. S18, ESI†). As soon as **NI-COF** is incubated with the HeLa cells, a notable difference is observed between cells exposed to hypoxia and those incubated under normoxic conditions. Under the same conditions of incubation with **NI-COF**, hypoxic cells exhibit a markedly increased fluorescence compared to the normoxic ones (Fig. S19, ESI†). These results show that **NI-COF** is not only able to serve as an imaging agent for severe cases of hypoxia with $[O_2] \approx 0\%$, but also for milder versions of hypoxia where $[O_2] \approx 5\%$. In contrast, **NO_2-COF** and **NH_2-COF** were unable to discriminate between the hypoxic and normoxic conditions (Fig. S20, ESI†). We anticipate that these results will stimulate further interest in the development of COFs for imaging specific cellular conditions, and for combined imaging and drug delivery applications.

This project has received funding from the European Union's Horizon 2020 research and innovation programme under the Marie Skłodowska-Curie grant agreement No. 101038091. DS acknowledges the financial support from the Khalifa University faculty startup grant (FSU-2020), and support under the Advanced Materials Chemistry Center (AMCC), Khalifa University, Abu Dhabi, UAE. M. V. and G. M. acknowledge financial support from the Slovenian Research Agency (research core funding No. P2-0412 and P1-0021, respectively).

Conflicts of interest

There are no conflicts to declare.

References

1 Q. Cai, T. Yu, W. Zhu, Y. Xu and X. Qian, *Chem. Commun.*, 2015, **51**, 14739–14741.
2 W. Piao, S. Tsuda, Y. Tanaka, S. Maeda, F. Liu, S. Takahashi, Y. Kushida, T. Komatsu, T. Ueno, T. Terai, T. Nakazawa, M. Uchiyama, K. Morokuma, T. Nagano and K. Hanaoka, *Angew. Chem., Int. Ed.*, 2013, **52**, 13028–13032.
3 P. Vaupel, F. Kallinowski and P. Okunieff, *Cancer Res.*, 1989, **49**, 6449–6465.
4 P. Bonnitcha, S. Grieve and G. Figtree, *Free Radicals Biol. Med.*, 2018, **126**, 296–312.
5 R. Kumari, D. Sunil, R. S. Ningthoujam and N. A. Kumar, *Chem. – Biol. Interact.*, 2019, **307**, 91–104.
6 S. Li, F. Huo and C. Yin, *Chem. Commun.*, 2022, **58**, 12642–12652.
7 E. Roussakis, Z. Li, A. J. Nichols and C. L. Evans, *Angew. Chem., Int. Ed.*, 2015, **54**, 8340–8362.
8 T. Skorjanc, F. Benyettou, J.-C. Olsen and A. Trabolsi, *Chem. – Eur. J.*, 2017, **23**, 8333–8347.
9 M. H. Y. Cheng, Y. Mo and G. Zheng, *Adv. Healthcare Mater.*, 2021, **10**, 2001549.
10 G. Das, F. Benyettou, S. K. Sharama, T. Prakasam, F. Gándara, A. Victor, N. Saleh, R. Pasricha, R. Jagannathan and M. A. Olson, *Chem. Sci.*, 2018, **9**, 8382–8387.
11 J. Zeng, X. Wang, B. Xie, M. Li and X. Zhang, *Angew. Chem., Int. Ed.*, 2020, **59**, 10087–10094.
12 P. Gao, X. Shen, X. Liu, Y. Chen, W. Pan, N. Li and B. Tang, *Anal. Chem.*, 2021, **93**, 11751–11757.
13 P. Gao, X. Shen, X. Liu, B. Cui, M. Wang, X. Wan, N. Li and B. Tang, *ACS Appl. Mater. Interfaces*, 2021, **13**, 41498–41506.
14 P. Wang, F. Zhou, C. Zhang, S. Y. Yin, L. Teng, L. Chen, X. X. Hu, H. W. Liu, X. Yin and X. B. Zhang, *Chem. Sci.*, 2018, **9**, 8402–8408.
15 Y. Jia, Y. Shen, Y. Zhu and J. Wang, *Spectrochim. Acta, Part A*, 2022, **272**, 121002.
16 S. Chandra, S. Kandambeth, B. P. Biswal, B. Lukose, S. M. Kunjir, M. Chaudhary, R. Babarao, T. Heine and R. Banerjee, *J. Am. Chem. Soc.*, 2013, **135**, 17853–17861.
17 K. Okuda, Y. Okabe, T. Kadonosono, T. Ueno, B. G. M. Youssif, S. Kizaka-Kondoh and H. Nagasawa, *Bioconjugate Chem.*, 2012, **23**, 324–329.
18 S. P. S. Fernandes, P. Kovar, M. Psenicka, A. M. S. Silva, L. M. Salonen and B. Espina, *ACS Appl. Mater. Interfaces*, 2021, **13**, 15053–15063.
19 M. S. Lohse, T. Stassin, G. Naudin, S. Wuttke, R. Ameloot, D. De Vos, D. D. Medina and T. Bein, *Chem. Mater.*, 2016, **28**, 626–631.
20 S. S. Thavamani and T. P. Amaladhas, *J. Mater. Environ. Sci.*, 2016, **7**, 2314–2327.

